Icarus 250 (2015) 294–307

Contents lists available at ScienceDirect

Icarus

journal homepage: www.elsevier.com/locate/icarus

Uranus' southern circulation revealed by Voyager 2: Unique characteristics

Erich Karkoschka *

Lunar and Planetary Lab, University of Arizona, Tucson, AZ 85721, United States

ARTICLE INFO

Article history:
Received 11 August 2014
Revised 27 November 2014
Accepted 1 December 2014
Available online 6 December 2014

Keywords:
Uranus
Uranus, atmosphere
Image processing
Data reduction techniques

ABSTRACT

Revised calibration and processing of 1600 images of Uranus by Voyager 2 revealed dozens of discrete features south of −45° latitude, where only a single feature was known from Voyager images and none has been seen since. Tracking of these features over five weeks defined the southern rotational profile of Uranus with high accuracy and no significant gap. The profile has kinks unlike previous profiles and is strongly asymmetric with respect to the northern profile by Sromovsky et al. (Sromovsky, L.A., Fry, P.M., Hammel, H.B., de Pater, I., Rages, K.A. [2012]. Icarus 220, 694–712). The asymmetry is larger than that of all previous data on jovian planets. A spot that included the South Pole off-center rotated with a period of 12.24 h, 2 h outside the range of all previous observations of Uranus. The region between −68° and −59° latitude rotated almost like a solid body, with a shear that was about 30 times smaller than typical shears on Uranus. At lower latitudes, features were sheared into tightly wound spirals as Voyager watched. The zone at −84° latitude was exceptionally bland; reflectivity variations were only 18 ppm, consistent with a signal-to-noise ratio estimated at 55,000. The low noise was achieved by smoothing over dozens of pixels per image and averaging 1600 images. The presented data set in eight filters contains rich information about temporal evolution and spectral characteristics of features on Uranus that will be the basis for further analysis.

1. Introduction

On the jovian planets, winds blow mostly eastward or westward, similar throughout each zone. The wind speed or rotational period as function of latitude characterizes the circulation of the planet. The first data point on the circulation patterns of the jovian planets was Jupiter's Great Red Spot tracked by Cassini in 1665. Further observations established Jupiter's and Saturn's eastward equatorial jets. Voyager 1 and 2 provided large data sets between 1979 and 1989. The spacecraft Galileo and Cassini, as well as the Hubble Space Telescope (HST) and ground-based telescopes complemented data since. Today, we know most of the four, jovian circulation profiles through tracking features at visible or near-infrared wavelengths.

Profiles have remained remarkably constant (e.g. Simon-Miller and Gierasch, 2010 for Jupiter, García-Melendo et al., 2011 for Saturn, and Sromovsky et al., 2012 for Uranus). Most noticeable was a decrease of Saturn's equatorial jet (Barnet et al., 1992). Some areas have a measured wind speed variation with altitude (e.g. García-Melendo et al., 2011 for Saturn). In this work, we do not focus on variations with time or altitude, but on latitudinal coverage.

Jupiter's and Saturn's profiles are completely known except for small gaps close to poles due to poor observing geometries (Fig. 1). Uranus' and Neptune's coverage is ~75% with large gaps south of −45° latitude for Uranus and north of +45° for Neptune.

The large gaps have different reasons. Neptune's sub-solar latitude has been close to −30° for many decades (cf. Fig. 1), which has made the region north of 45° unobservable or too foreshortened to track features. On the other hand, Uranus southern latitudes have been imaged thousands of times with great geometry, but Uranus seems to be bland south of −45° latitude.

The observing geometry for Neptune's gap is improving but Uranus' gap will remain in darkness for several decades (Fig. 1). During the next decades, Neptune's gap can be filled with new observations, but filling Uranus' gap can only be done with past data. Uranus' profile also has a small gap north of 78° latitude that is due to poor observing geometry during the past decades, but this area is just getting well observable.

Voyager 2 imaged Uranus near its 1985 winter solstice with unsurpassed spatial resolution. Images showed seven discrete features, an order of magnitude less than for other Voyager fly-bys of jovian planets (Smith et al., 1986). Their Fig. 8 summarizes the

* Fax: +1 (520) 621 4933.
E-mail address: erich@lpl.arizona.edu

http://dx.doi.org/10.1016/j.icarus.2014.12.003
0019-1035/

Voyager rotational profile. It contains eight data points since one large feature was centered at two different latitudes in different filters. The single feature south of −45° latitude was weak. It was mentioned at −70° latitude with a 14.2 h rotational period, but plotted at −71° with a 14.3 h period (if these latitudes are planetocentric, they correspond to −71° and −72° planetographic that are used in this work). No discrete feature south of −45° latitude has been seen since.

The first HST images of Uranus were almost bland (Hammel, 1997; Karkoschka, 1997). Later images at wavelengths beyond 1 μm revealed features of high contrasts (Karkoschka, 1998). Adaptive optics at Keck captured features from the ground (Sromovsky et al., 2000; Sromovsky and Fry, 2005) and has provided most circulation data since. The data suggest a smooth rotational profile with a slow-rotating equator and fast-rotating high latitudes (Sromovsky et al., 2009, 2012).

Rotational profiles of jovian planets are almost symmetric with respect to the equator (Fig. 1). The asymmetry is an important parameter since it suggests whether winds on both hemispheres may be connected through the interior or are limited in depth. Uranus became the last jovian planet with data about rotational asymmetry (Karkoschka, 1998), refined by data with improved coverage (Sromovsky et al., 2012). The thin lines of Fig. 2 show the current status, excluding this work. For Jupiter, Saturn, and Uranus, root-mean-square (rms) asymmetries are 0.3%, 0.7%, and 0.5%, respectively. Neptune's data allow similar asymmetries including symmetry. Even Uranus' lonely data point at high southern latitudes shows a similar asymmetry (Fig. 2). Thus, all current data suggest that asymmetries are on the order of half a percent, so that Uranus' asymmetry might be similar even in the data gaps.

The thick curve of Fig. 2 takes the result of this work up front and contradicts these expectations. Our profile between −47° and −78° compared with Sromovsky's northern profile gives a 2% rms asymmetry, the largest asymmetry among jovian planets. If Sromovsky's extrapolation of a flat profile north of 78° latitude is roughly correct, the asymmetry near Uranus' poles is well beyond 10%.

The thick curve is based on tracking dozens of features, based on the same Voyager images that revealed only a single feature

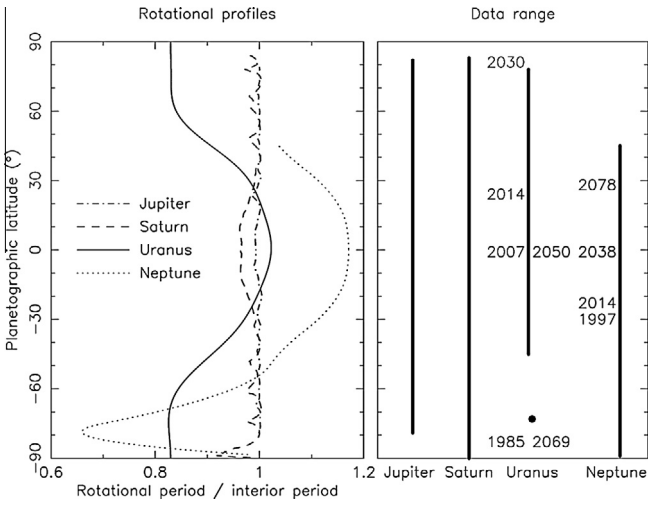

Fig. 1. Rotational profiles of the jovian planets normalized to interior periods (left) and the latitudinal range of data (right). Sub-solar latitudes for selected years are indicated for Uranus and Neptune. Data were taken from Limaye (1986) and Barrado-Izagirre et al. (2008) for Jupiter, from García-Melendo et al. (2011) for Saturn, from Sromovsky et al. (2012, best fit, even + odd using 1997–2011 data) for Uranus, and from Limaye and Sromovsky (1991), Sromovsky et al. (1995), and Karkoschka (2011) for Neptune.

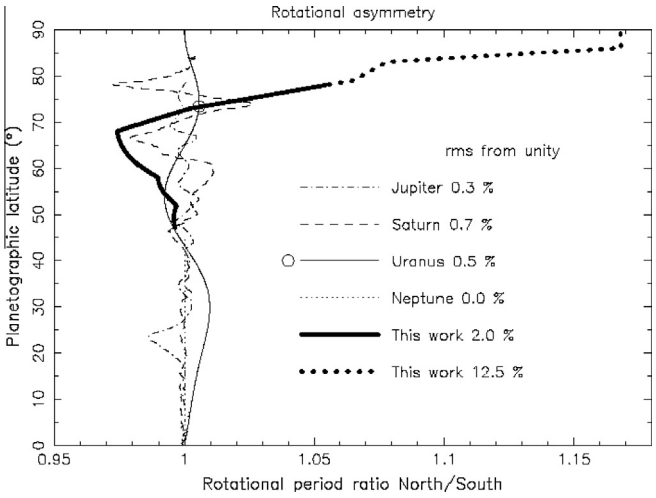

Fig. 2. North–south asymmetry of the rotational profiles of the jovian planets. Thin lines are from previous work (cf. Fig. 1). A data point for Uranus is indicated by a circle. The thick line is from this work. Its dotted section beyond 78° is uncertain due to the lack of data for the northern hemisphere.

Table 1
Key processing methods.

Section	Method
2.3	Determination of detector nonlinearity curves as function of filter
2.4	Reduction of flatfield noise with the help of averaged Uranus images
2.5	High-fidelity interpolation of missing data, in particular resau marks
2.11	Elimination of large-scale detector instability
2.14	High-pass filtering to eliminate medium-scale detector instability
2.16	Averaging rotated images in order to dramatically reduce noise
4.1	Automated correlation method to track faint discrete features

before. A revised calibration presented here allowed more accurate measurements of that feature, but discovering all the other features required new image processing methods. Thus, the critical part of this work is image calibration and processing, described in the next section. Table 1 lists key methods that were essential. Sections 3 and 4 describe rotational measurements with manual feature tracking and with a correlation method, respectively. Section 5 focuses on a feature far off the expected rotational profile. Section 6 discusses a region with an untypical rotational shear. Section 7 mentions unusual features. Section 8 lists animations available in the online version. A summary concludes this work.

2. Image calibration and processing

2.1. Data selection

All usable images were selected since results improve with the amount of data. We excluded Uranus images taken after closest approach since they show a thin crescent with no significant detail. Images with a diameter of Uranus of less than 100 pixels were also excluded.

Images with large areas of missing data, including saturation, were excluded, also when most of the disk was outside the field of view. Long exposures with a significant smear due to imperfect tracking were excluded where the smear length was more than 7% of Uranus' radius.

These selection criteria left a total of 1600 images that are the basis for this work. Table 2 lists a summary of their parameters. The observations occurred in seven periods, called periods P1

Table 2
Voyager observation periods of Uranus.

Period	Date 1985/1986	Camera	Diameter (pixels)	# of images
P1	Dec 18.6–20.1	NAC	119–124	243
P2	Dec 27.6–29.1	NAC	157–166	277
P3	Jan 04.8–06.1	NAC	226–237	240
P4	Jan 10.5–11.8	NAC	310–340	239
P5	Jan 13.6–15.3	NAC	394–465	286
P6	Jan 16.6–18.6	NAC	539–718	105
P7	Jan 21.1–24.1	WAC	159–869	210

through P7 in this work. Each period consists of almost continuous imaging for about a couple of days. In between periods are long gaps of other spacecraft activity.

Uranus apparent size increased by a factor of 55 within this data set. For best resolution, the first six periods used the Narrow Angle Camera (NAC) while P7 used the Wide Angle Camera (WAC) with a 7.5 times smaller focal length and scale to capture the whole planet. Both cameras had detectors of 800 × 800 pixels.

Both cameras had Violet, Blue, Green, and Orange filters. Additionally, the NAC had a ultraviolet filter (UV) and provided unsaturated images with the Clear filter, while the WAC had two narrow filters for the 543 and 619 nm methane bands. Both filters at the spectral ends (UV and CH4_JS) had low sensitivity and provided noisy images that were only useful for some aspects of this work. Both NAC Green filters were almost identical and thus treated separately only in the calibration. Each filter is listed in Table 3 with its effective wavelength, width, and methane absorption coefficient, and the average signal-to-noise ratio for pixels on Uranus.

For each exposure, the apparent size of Uranus and the sub-spacecraft and sub-solar longitudes and latitudes were taken from the JPL's Horizons ephemeris calculator (http://ssd.jpl.nasa.gov/horizons.cgi). The sub-spacecraft latitude varied between −73° and −66°, the sub-solar latitude was constant at −82.1°, and the phase angle varied between 14° and 21°.

2.2. Preprocessed data

Voyager images are stored on the Rings Node of the Planetary Data System (PDS) in four different calibration stages: raw, cleaned, calibrated and undistorted (Showalter et al., 2013). Raw images contain the original data numbers between 0 and 255. In cleaned images, data numbers of pixels with clearly bad or missing data were replaced by interpolated values from nearby pixels. Calibrated images were subtracted with dark frames, corrected for the nonlinear response, divided by a flatfield, and scaled to reflectivity I/F using a calibration constant for each filter. Data numbers were multiplied by 10,000 before being rounded to integers. Geometrically calibrated images have the distortion of the camera removed using measured locations of reseau marks. Details are described in Benesh and Jepson (1978) and Danielson et al. (1981). This work is based on the calibrated images as the starting point with additional usage of cleaned images.

2.3. Nonlinearity

In contrast-enhanced, high-pass filtered images of Uranus, we found artifacts in calibrated images that are not present in cleaned images: dark, narrow rings that roughly run along isophotes and are about 1% darker than the surroundings. They stand out well because most features on Uranus are of lower contrast.

These artifacts are best aligned with isophotes when the flatfielding is reversed. This suggests that these rings were introduced in the nonlinearity transformation, which was created in the 1970s and stored on files in an old format that is not readable any more (Showalter, private communication). Nonlinearity curves from laboratory measurements are documented in Benesh and Jepson (1978), but the figures are insufficient to measure the correction to 1%. In order to understand the nonlinearity, we tried to reproduce it based on cleaned and calibrated images.

We determined the implemented dark subtraction by comparing the background data numbers off the disk of Uranus in cleaned and calibrated images. We found the implemented dark subtraction to be almost as described in the documentation (Showalter et al., 2013), except that dark images were slightly modified during certain time periods to improve the result. We used this dark subtraction for the determination of nonlinearity, but we slightly adjusted it in our revised calibration according to median data numbers of the sky background in each image.

Using dark-subtracted and calibrated images, we could determine either flatfields or nonlinearity corrections. Since neither was known, we used an iteration, separately for each filter and camera. First, we assumed that the detector is linear for low exposure levels. This provided the flatfield at all pixels where at least one of the typically hundreds of images had low exposure levels. The next iteration found nonlinearity at higher exposure levels and a more complete flatfield, etc. The end of the iteration yielded the implemented flatfield and the nonlinearity correction. In each image, the nonlinearity correction was the same for all pixels with the same dark-subtracted data number. Nonlinearity functions are very dependent on the filter (Fig. 3).

For NAC exposures with data numbers above 200, the curves also vary significantly from one image to the next one. We checked whether this was real, but the camera was close to stable. Constant nonlinearity curves yielded almost stable geometric albedos of Uranus while the implemented curves made it jump up and down. Thus, we adopted constant nonlinearity curves.

Table 3
Filters of the Voyager 2 imaging cameras.

Camera	Name	Eff. wavel. (nm)	Width (nm)	Eff. CH_4 (km-am^{-1})	Mean S/N	# of images
NAC	UV	388	49	0.000	55	180
	Violet	411	80	0.000	186	200
	Clear	480	227	0.012	204	323
	Blue	482	100	0.005	188	197
	Green #6	564	98	0.037	175	170
	Green #5	567	93	0.039	178	158
	Orange	592	65	0.055	123	162
WAC	Violet	431	53	0.000	224	10
	Blue	474	97	0.004	237	14
	Green	564	94	0.036	220	24
	Orange	599	58	0.073	208	28
	CH4_U	542	13	0.072	211	62
	CH4_JS	621	15	0.36	33	72

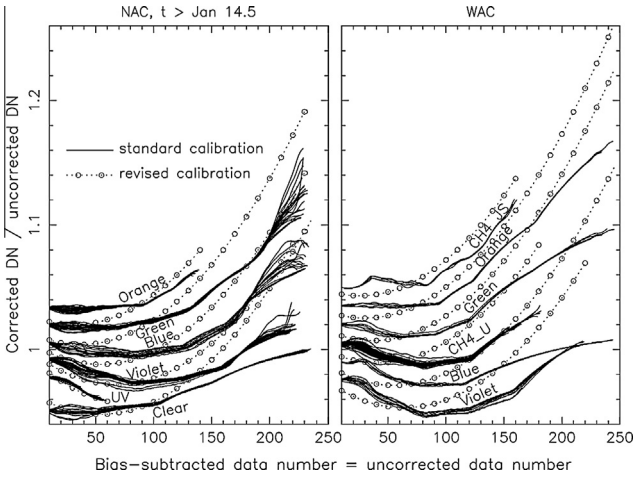

Fig. 3. Nonlinearity of the NAC and WAC cameras in six filters each. Solid curves are from measurements in individual cleaned and calibrated images, using images with long exposure times only. Dotted lines show the revised calibration of this work. The minima are offset for different filters to avoid overcrowding.

Fig. 3 shows the nonlinearity curves composed of almost linear sections with kinks in between. The sections become perfectly linear in a plot with the corrected data number as the ordinate. The isophotes corresponding to the kinks appear dark because they are darker than the average of data points on both sides of the kink. This explains the spurious artifacts of dark rings. Therefore, we adopted nonlinearity curves that are smooth without kinks.

Finally, we determined the slopes of nonlinearity curves using exposures on Uranus, while the implemented version used laboratory exposures. For each filter, exposure times on Uranus typically alternated between two values with a ratio of either 3:2 or 4:3. The lower exposure time was safe from saturation while the higher one provided lower noise in non-saturated areas. The longer exposures provided albedos consistently several percent lower than the shorter ones. This implies that the slopes of nonlinearity curves were underestimated in the implementation.

We adjusted the nonlinearity curves by trial and error and plotted the histogram of the number of pixels brighter than each reflectivity level, separately for both exposure times. For each filter, we could match the pair of histograms with a quadratic nonlinearity function by adjusting two parameters of the function. The third parameter, the scale factor for absolute intensity, was normalized to unity at the minimum of the curve. The minimum signifies where the response is proportional to illumination.

The curvature parameter was the same for all filters within our precision. The slope parameter was dependent on the filter wavelength, but similar for both cameras. A linear dependence with wavelength worked satisfactorily. Thus, our adopted nonlinearity function is:

$$\mathrm{DN}_{\mathrm{corrected}}/\mathrm{DN} = 1 + 5 \times 10^{-6}[\mathrm{DN} + \lambda/5 - 150]^2 \quad (1)$$

where DN is the dark-subtracted data number, $\mathrm{DN}_{\mathrm{corrected}}$ is proportional to illumination, and λ is the effective wavelength of the filter in nanometers. This function is shown as dashed curves in Fig. 3. It has two characteristics: (1) the slope increases with wavelength; (2) the curve's minimum occurs at higher data numbers for filters of shorter wavelengths.

Implemented nonlinearity curves have the same characteristics, indicating qualitative agreement. However, the variation between low and high exposure levels is in disagreement by 5–10%. Our spectral variation is smooth, while the implemented version has a jagged spectral variation. For example, the WAC Blue filter has shallower solid curves than filters of shorter and longer wavelengths. Our curves have the same curvature while the implemented curves have variable curvature without a consistent trend. Our curves for both cameras at identical wavelengths are the same, but they are significantly different in the implementation (Fig. 3).

Based on the comparison of histograms, we estimate our nonlinearity functions to be 5–10 times more accurate than the implemented ones. This reduces previous errors in relative reflectivity of 5–10% down to about 1%. This is important for Uranus, but other Voyager images might benefit from this improvement too. A calibration to 5–10% was state of the art in the 1970s, when the standard calibration was implemented, but today we can do better.

2.4. Flatfield noise

By monitoring details at high spatial frequencies from image to image, we realized that they were mostly stationary with respect to pixel location, but not moving with Uranus, as expected for features on Uranus, nor random, as expected for noise in the Uranus exposures. This structure must come from imperfect flatfields. Indeed, most bright pixels on Uranus are faint ones in flatfields and vice versa.

Flatfields had to be underexposed by a factor of ~2 in the center of the field in order to avoid saturation in the corners. On the other hand, most images of Uranus were exposed near the center with exposure levels close to the saturation level. This way, the Uranus images ended up with higher signal-to-noise ratios than their flatfields.

We created low-noise flatfields using Uranus images. For each filter, we added up all ~200 images of Uranus. We used a high-pass filter to remove large-scale variations mainly due to limb-darkening of Uranus. Since the small-scale structure of flatfields was similar in filters of the same camera, we averaged over most filters, while the two filters at the extreme ends of the spectrum (UV and CH4_JS) got individual consideration. For the 72 images of filter CH4_JS, we removed the strongest features on Uranus by interpolation from surrounding pixels for the flatfield modification. We confined changing flatfields to scales up to 20 pixels.

Uranus may not be as flat as a flatfield screen, but averaging some 1000 images reduced features on Uranus to insignificance. This process worked since Uranus jumped randomly in the field of view due to imperfect tracking, unlike data sets where all images are centered. Our flatfields are about an order of magnitude less noisy than the original ones on a scale of 10 pixels.

The NAC images of Uranus contain small stationary dark rings that may be out-of-focus images of new dirt in the camera after the flatfields were taken. We measured the most significant 31 of them and removed them initially. Their radii are 6, 14, or 21 pixels, and their intensity contrasts are between 0.2% and 1.8%. Some are visible in the left panel of Fig. 4.

The calibrated images for the NAC Green filter in filter wheel position #5 show intensity gradients on Uranus with column number that are unphysical and large (>10% across the field). We concluded that the calibration used the #6 flatfield for images in the #5 filter. We created a correction flatfield for the #5 filter that made the unphysical effect disappear.

2.5. Bad pixels

The cleaned images are greatly improved with respect to original images. For example, the 100% original intensity error at reseau marks is typically reduced to about 1%. We improved the interpolation by another order of magnitude using a refined method. Also, near the limb of Uranus, our interpolation direction was along arcs parallel to the limb of Uranus to avoid strong intensity gradients from limb darkening that caused the original interpolation algorithm to perform poorly. We further added a finer method to detect

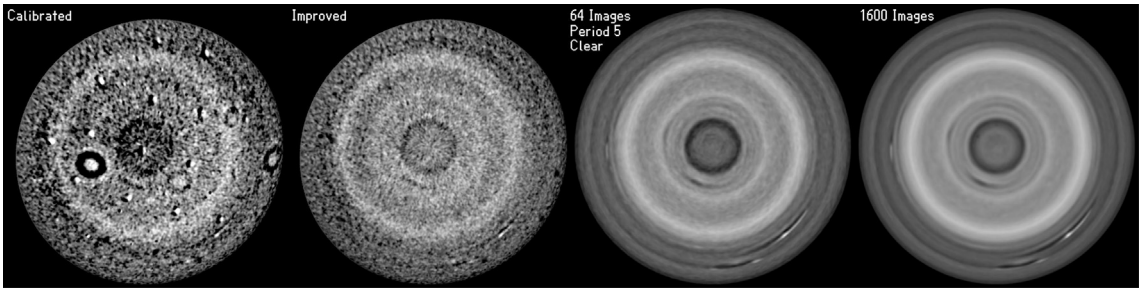

Fig. 4. The image #2654719 in four different stages. All four images went through a high-pass filter before being displayed at 200-times enhanced contrast. They are projected as seen from above the South Pole. At the left is the calibrated version available from the PDS. Next is the revised calibration as described in Sections 2.3 through 2.14. The third image is the average for all Clear-filter images of period P5 as described in Section 2.16. The last image is an average using all 1600 images.

outliers. We individually adjusted interpolation parameters based on critical evaluation of each image. About 1% of the more than 100 million data points on Uranus were interpolated due to all the reasons combined.

We measured the noise characteristics of each pixel by comparing its data numbers with respect to its neighbors throughout all images. We found 309 pixels of the NAC and 45 pixels of the WAC which were much noisier than the rest of the pixels. We interpolated their data.

We investigated instrumental patterns. For example, the images of period P1 display a pattern that repeats every 12 columns with an amplitude of 0.1% in intensity. We measured this pattern by combining all Uranus data of period P1 and then removed it.

Where Uranus hit the edge of the field of view, especially in WAC images, data numbers were higher than expected. We flagged inconsistent data so they would not be used further.

Our calibration improvements are shown in the second image of Fig. 4. Features are not dominated by artifacts any more, and the noise is lower than in the first image.

2.6. Saturation

We investigated data close to the saturation level (typically data number 254 or 255) and found features to be dominated more and more by artifacts the closer data numbers approach the saturation level. Thus, we considered all raw data points with data numbers of 250 and above as saturated, except single pixels where all four neighbors had data numbers of less than 250 which allowed reliable interpolation. Saturated areas were flagged and not used in the further analysis.

2.7. Navigation of the disk center

The Voyager imaging cameras have strong distortions. Most significant is the barrel distortion. Next in line is a scale difference with direction. In the NAC images, Uranus is extended in the x-direction by 0.5% and compressed in the perpendicular direction by 0.5%. For the WAC images, this distortion is 0.7% and rotated about 45° clockwise with respect to the NAC case. Also, Uranus appears up to about 0.4% larger in long exposures compared to short exposures. We measured these distortions using the method described below. More complicated distortions in the corners of the field of view, affecting only little data, were neglected.

With phase angles of 14–21°, all images of Uranus have a very sharp, illuminated limb around 180° of the circumference that we used for the navigation. A routine measured the location of the strongest radial gradient of the intensity for 900 position angles, every 0.2°, which was compared to the calculated shape of the limb. This provided the pixel location of the center of Uranus. Differences unexplained by our adopted distortion were 0.28 pixels rms, which is an estimate for the precision of the navigation.

In 1% of the images, most of the illuminated limb of Uranus was outside the field of view so that both navigation coordinates had to be estimated by a manual comparison with other Uranus images. For another 4% of the images, one coordinate had to be estimated that way while the other one was reliably determined by the routine.

2.8. Image smear

Many long exposures, in particular those taken with the NAC, are smeared due to imperfect tracking. In order to measure the smear length, the routine locating the bright limb of Uranus also measured the sharpness of the limb as function of position angle. The full-width-half-maximum (FWHM) data of the radial intensity gradient were fitted to a sine curve with a period of 180°. The minima and maxima indicated the size of point spread function and the PSF plus smear, respectively.

Almost 10% of all images, those with a PSF plus smear of more than 7% of the radius of Uranus, were rejected, mostly images with poor image scale. For the remaining images, the smear parameter was used in further analysis for data weighting.

Calibrated images display a weak checkerboard pattern. It was reduced by a low-pass filter: adding 10% of each of the four neighbor data numbers to 60% of the central-pixel value.

2.9. Navigation of position angle

Zonal features allow accurate navigation of the position angle of the rotational axis, although this is more difficult with high sub-spacecraft latitudes, in our case around −70°, and with a planet that displays sharp zonal features only in averaged images. We first assumed a position angle and projected images onto a longitude–latitude grid. The angle was adjusted until zones ran horizontal along latitude circles. We determined the counterclockwise rotation angle PA needed to upright Uranus' North Pole as two functions:

$$\mathrm{PA} = 32.3^\circ + 0.26^\circ D + (27/D)^2 \quad t < \text{1986-01-22.5} \tag{2}$$

$$\mathrm{PA} = 100.0^\circ - 0.13^\circ D \quad t > \text{1986-01-22.5} \tag{3}$$

where t is the observing date and D is the diameter of Uranus in pixels for the WAC, which is 7.47 times smaller than the diameter in the NAC. We estimate that this position angle is accurate to about 0.5°. This implies that retrieved latitudes are accurate to 0.2° in a single image, and better in averaged images. A relative error of 0.5° in position angle between the first and last observations is small compared to the 18,000° of 50 rotations of Uranus during that interval. This causes a systematic error of retrieved rotational periods of only 0.003%.

2.10. Sub-spacecraft latitude adjustment

The sub-spacecraft latitude is defined here as the angle between the line from the center of Uranus to the spacecraft and the equatorial plane of Uranus. It varied slightly. We created a data set with identical sub-spacecraft latitudes to simplify further work by shifting each data point parallel to the rotational axis. The shift length was determined by projecting an image onto a longitude–latitude grid and re-projecting it with the desired sub-spacecraft latitude. We chose a sub-spacecraft latitude of −72.5° for the NAC images and −69.5° for the WAC images. The actual sub-spacecraft latitudes differed by 0.1° rms for the NAC images and by 1.2° rms for the WAC images. We included a slight radial translation so that the image geometry corresponds to a viewing distance approaching infinity. Both shifts were typically less than 1 pixel.

2.11. Camera instability

The Voyager cameras did not produce perfectly stable intensity measurements. Measured geometric albedos typically varied by about 1%, and relative intensities across the disk also varied by about 1%. We measured the large-scale intensity variations using five parameters, one for the total intensity, two for intensity gradients, and two for second-order terms. We removed these variations leaving the average of all images of the same filter unchanged.

2.12. Resampling

Considering the image scale, the distortions of the camera, the three navigation constants, and the adjusted sub-spacecraft latitude, all images were resampled using cubic interpolation to center Uranus in the frame and scale the equatorial radius of Uranus to 390 pixels, with north on Uranus pointing up. This image set, called the revised calibration, is generally sub-sampled.

2.13. Limb-darkening fit

For each filter of each camera, all images of the revised calibration were averaged. We performed a least-square fit to each averaged image assuming the reflectivity function:

$$I/F = \mu_0[A + B/(\mu + \mu_0) + C/(\mu + \mu_0)^2] \quad (4)$$

where μ and μ_0 are the cosines of the observed and solar zenith angles, and A, B, and C are the three adjustable parameters for each filter. The case $B = C = 0$ is the Lambert Law, the case $A = C = 0$ is the Lommel Seeliger Law, and the case $A = B = 0$ corresponds to limb brightening. Data points close to the limb got reduced weights due to dependence on image smear.

For each filter, we generated a synthetic image using the fitted parameters and smoothed it slightly to roughly match the observed sharpness of the limb. We subtracted this image from each revised calibrated image. The subtracted images have small ranges of data numbers, on the order of 0.01 in I/F, so that displays catch the main features.

These images show low and high latitudes in similar brightness, although it is impossible to decide whether both regions were physically similar since they were observed at different geometries. A decade later, lower sub-observer latitudes made this possible, and low latitudes were significantly darker than the polar region at most wavelengths (Karkoschka, 2001).

2.14. High-pass filtering

After we subtracted the limb darkening fit, it became apparent that images still showed minor intensity variations on medium scales due to spatial camera instability. We removed them by high-pass filtering, by smoothing the images and then subtracting the smoothed image. For the center of the disk, we used a Gaussian profile for the smoothing operation. Toward the limb of Uranus, the method worked best by squashing the smoothing profile in the radial direction so that the smoothing near in limb occurred mostly along an arc parallel to the limb.

We created two data sets with two different amounts of high-pass filtering. The moderate high-pass filtering used a Gaussian with about 100 pixels FWHM. Thus, all spatial frequencies with wavelengths above about 100 pixels are removed. This corresponds to about 6000 km on Uranus or 15° in latitude near the center of the disk. The strong high-pass filtering had a FWHM of 40 pixels, so that all spatial information on scales larger than 2500 km or 6° is removed. The cut-off in frequency is not sharp but close to a Gaussian fall-off.

The strong high-pass filtering eliminated detector artifacts perfectly. The moderate filtering still showed unphysical features in images with original diameters of Uranus above 600 pixels, and weakly even to 400 pixels. Thus, the information of medium-scale features was retrievable from a partial set of all images. This suggests that the cameras performed perfectly to the photometric requirements of this work up to scales of almost 100 pixels in the original images.

High-pass filtering has the intrinsic characteristic that it creates dark halos around small, bright features and vice versa. This was generally a minor effect and only noticeable for strong features. We modified the high-pass filtering to decrease halos. We determined the average and sigma (rms) data numbers in the image with the strong high-pass filter. Then, data numbers were capped at 1.5 sigma above or below the average for the smoothing process.

High-pass filtered images have data numbers corresponding to reflectivity differences, which we describe as contrast values. For example, a feature with a contrast of +1% has a reflectivity 1.01 times the smoothed reflectivity.

2.15. Longitude–latitude grid

Each image in both high-pass filtered versions was projected onto a longitude–latitude grid. Data points too close to the limb ($\mu < 0.2$) or terminator ($\mu_0 < 0.1$) were not useful for the purpose of this work. The remaining data points, 96% of all data points, got attached with weights of $(\mu - 0.2)$ $(\mu_0 - 0.1)$ so that further analysis was mostly based on data points far from the limb. Data points close to saturated or missing data points had their weights further reduced so that the weight gradually decreased to zero toward the missing data. Furthermore, weights were multiplied by the data volume in original images, which is proportional to the square of the apparent radius of Uranus. Finally, weights were reduced by a factor of 1.5 for each smear increase of 1% of the radius of Uranus, corresponding to a weight factor around 10 between images of very high and low smear. For the two filters at the extreme end of the spectrum, the factor 1.5 was changed to 1.2 since smear was less important there.

For the projected images, the adopted sampling in latitude was similar to that on the central meridian in the revised calibrated images. In longitude, the sampling was 0.6°/pixel, which corresponds to about three original pixels near the equator for the images of highest resolution. The lost information about the highest spatial frequencies in the longitudinal direction was only significant for known features (Smith et al., 1986), but not for the weaker

features revealed here. In order to use all information, unprojected images were first smoothed by 3 pixels in longitude.

We also created projected images with four successive data points averaged in longitude for a longitudinal sampling of 2.4°/pixel. They allowed recognizing features spread out in longitude.

Areas of projected images around selected features are shown in Fig. 5. The center latitude of each panel is listed, and the center longitude was based on assumed rotational periods as listed. The sensitivity of the east–west centering on the assumed rotational period is shown in the bottom two rows of Fig. 5. The last but one row has the assumed rotational period reduced by 0.01 h, and the feature clearly moves from left to right over the periods P1 to P7. The opposite is the case for the same offset in the opposite direction (bottom row). This suggests that for significant features at low latitudes, rotational periods can be easily constrained to better than 0.01 h. At high latitudes, the accuracy is lower according to the factor $\cos\varphi$, where φ is the latitude.

Achieving higher accuracy is of little use. The accuracy of 0.01 h is already two orders of magnitude better than what is needed to support the main conclusions of this work. Furthermore, the rotational profile of Uranus is so steep that the accuracy of the rotational profile is limited by the accuracy of latitude measurements that are intrinsically difficult because the apparent location of some features depend on the wavelength of observation.

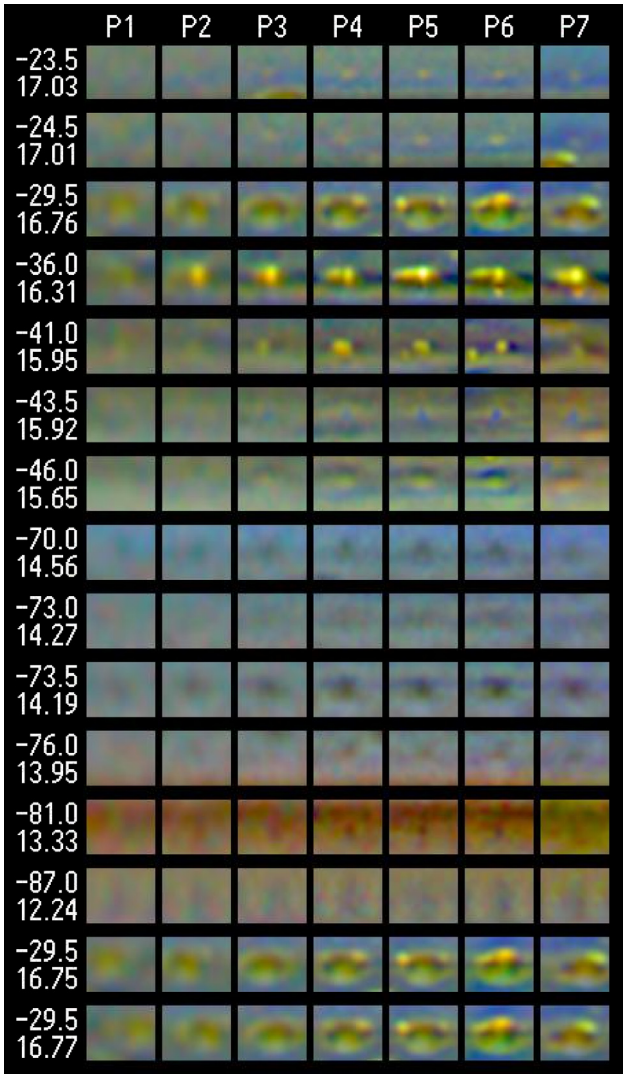

Fig. 5. The evolution of 13 selected features over the seven periods from left to right. Each panel is 1470 km wide and 280 km high and thus distorted to accommodate Uranus' typically elongated features. The center latitude of each panel and the assumed rotational period in hours for the east–west centering are listed at left. Some features are too weak to be visible during the early periods. The bottom two rows show the third feature, but with assumed rotational periods off by 0.01 h either way.

Fig. 5 suggests that most features were relatively stable during the five weeks of observations, although details within the features clearly move and change. Thus, rotational measurements are more reliable when they focus on a feature as a whole, but less reliable when they focus on a small detail, such as the brightest spot of a feature. This observation is important for automated measuring methods that will be introduced later.

2.16. Averaging images

Each image in the projected longitude–latitude grid version was "rotated" from the actual date to a central date adopted for each observing period, a horizontal shift in longitude. The shift length depends on the rotation period of Uranus' atmosphere as function of latitude. For the first iteration, we used the rotational profile of Sromovsky et al. (2012). This procedure was iterated with other rotational profiles until images averaged over a period displayed the sharpest features.

The average image for each period and filter produced a set of 41 images of reduced noise. Six filters for seven periods gives 42 cases, but the Clear filter was not used in period P6. One of the 41 images is shown as the third image in Fig. 4 as viewed from above the South Pole. This step is the single most important one of this work in revealing faint features.

We also created a set of images for 12 sub-periods considering that periods with better data need less averaging to reveal the same features. Periods P4, P6, and P7 were divided into two sub-periods, and P5 into three sub-periods, while P1 through P3 remained unchanged.

Considering observed spectral characteristics of many features, we used spectral averaging to further reduce noise. Averages over Violet, Clear, and Blue filters are called Violet–Blue images, averages over Green, Orange, and CH4_U filters are called Yellow images. The weighting was according to the number of images per filter. Averaging both spectral regions decreased the noise further for some features, and even more so by averaging over several periods. An extreme example is displayed in the right-most panel in Fig. 4 where all 1600 images were averaged. Here, the weighting of different filters occurred according to the spectral sensitivity of the Clear filter. Of course, too much temporal averaging can smear out some features. Another averaging example is Fig. 6 where all images of each filter were averaged.

3. Feature tracking

In averaged images, 27 features could be easily tracked through several periods. The 27 rotational periods are listed in Table 4. Fig. 7 shows these results in comparison with the profile from Sromovsky et al. (2012).

North of −57° latitude, the new data are consistent with Sromovsky's curve for the southern hemisphere. Six of these measurements correspond to features seen in 1986, and results are consistent as well. South of −57°, Sromovsky's curve goes through the only data point known before (at −73°), but the new measurements reveal a rotational profile that is very different. Other latitudes of Uranus and Neptune have a smooth profile, but the new data show kinks. Previous data on jovian planets suggested profiles close to symmetric between the south and north, unlike the new profile. The far-southern latitudes of Uranus have an unusual

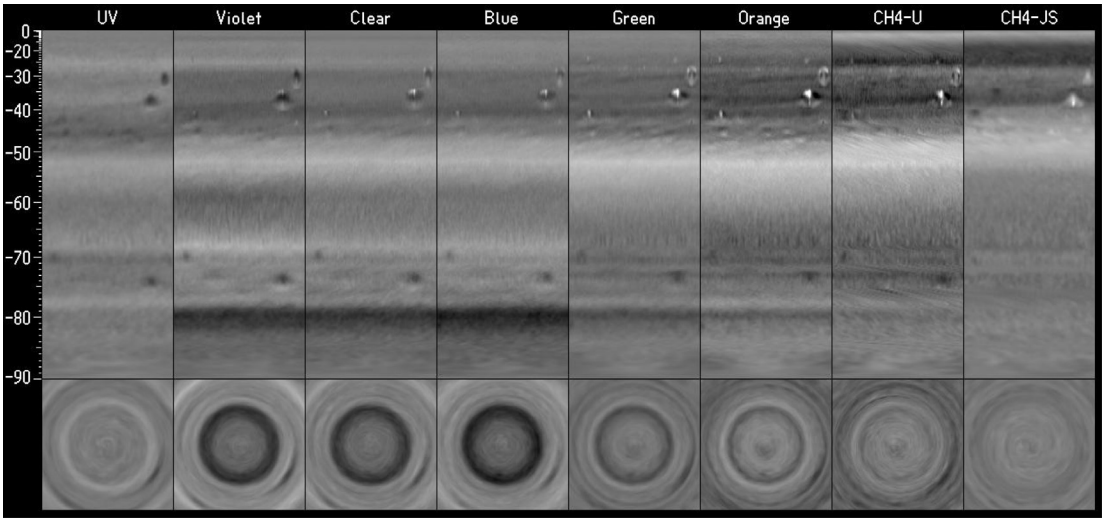

Fig. 6. Average images on a latitude–longitude grid for all eight filters at 1986-01-15.5. The zero meridian is in the center of each panel. The region around the South Pole is shown in polar projection below each panel. The contrast enhancement factor is 200, except 100 for the UV and 50 for the CH4_JS filter. Features that run from top left toward bottom right in both CH4 filters are artifacts due to the time change from late January to the standard date Jan 15.5.

Table 4
Measurements of the rotational period.

Latitude (°)	Feature tracking (h)	Correlation method (h)
−23.6	17.02	17.031
−24.0	17.01	17.029
−27.5	16.79	16.764
−27.5	16.76	16.764
−35.4	16.31	16.311
−41.0	15.96	15.961
−44.8	15.67	15.641
−44.8	15.67	15.641
−45.0	15.64	15.642
−46.5	15.51	15.640
−46.8	15.48	15.441
−47.8	15.45	15.482
−47.8	15.45	15.482
−49.0	15.31	15.333
−49.5	15.28	15.275
−50.5	15.25	15.284
−56.7	14.75	14.761
−57.5	14.75	14.746
−61.0	14.70	14.714
−64.5	14.70	14.707
−70.0	14.55	14.561
−72.5	14.28	14.204
−73.0	14.19	14.196
−75.8	13.95	14.200
−78.5	13.60	13.619
−81.2	13.32	13.325
−87.0	12.23	12.231

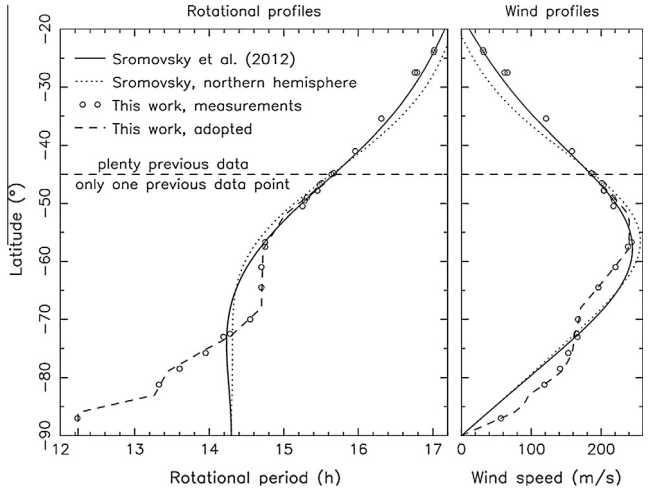

Fig. 7. Rotational data based on longitude measurements of discrete features (circles). For comparison, the Sromovsky et al. (2012) profile is shown as a solid curve, while their northern-hemisphere profile mirrored to the southern hemisphere is shown as the dotted curve. Most important are data points below the horizontal dashed line where only a single data point existed so far. The right panel displays the same data as wind speeds relative to a 17.24 h rotation, the best estimate for Uranus' interior rotation (Warwick et al., 1986).

rotational profile and only low-contrast features. Could both characteristics be related?

4. Correlation method

4.1. Rotational data

Aside from the 27 measured features, the averaged images show many features close to the noise limit that are difficult to reliably track from period to period. In such cases, correlation techniques have shown superior results, especially for the multitude of features seen on Jupiter and Saturn (e.g. García-Melendo et al., 2011). We created a routine measuring rotational periods using 24 images: the Violet–Blue and Yellow images for the 12 subdivided periods.

Results depend on the amount of spatial smoothing. With too little smoothing, the routine focuses on high-frequency noise and small details within major features that vary on short time scales (Fig. 5). With too much smoothing, real features are smoothed out beyond recognition. Best results occurred for a smoothing of 800 km FWHM in longitude and 200 km FWHM in the radial direction in an image of polar projection (1° of latitude = 450 km).

The routine lined up all observations according to 800 different rotational periods, every 0.01 h from 11 to 19 h. For each rotational period, the routine averaged all images according to weights derived from each observation. For each latitude, the longitudinal intensity profile was determined. The rms deviation of the intensity is a measure of the signal, and the square-root of the sum of squares of the rms deviations for Violet–Blue and Yellow is a measure of the total signal. A zone without real features gives a similar

signal for all 800 rotational periods. Real features cause a spike at their rotational period. The routine excelled at determining rotational periods for latitudes with many features of similar contrasts.

An example is shown in Fig. 8 for latitude −67° and just 11 of the 800 rotational periods considered. In the top half, the longitudinal profiles for the 12 sub-periods are lined up according to an assumed rotational period of 14.70 h. For an assumed rotational period of 14.65 h, the first and last profile would be shifted by 70° with respect to each other, and for value of 14.75 h, the shift would be the same but in the opposite direction. The profiles show features on the order of ±0.05% contrast, i.e. a reflectivity between 0.9995 and 1.0005 times the smoothed reflectivity in the surrounding area. Even though each profile is based on typically more than 100 images and thus about 10 times less noisy than the data of a single exposure, each profile looks like it might be simply noise. There is no outstanding feature in any single profile that is clearly above the noise level. Thus, the method measuring longitudes of features cannot be applied here. Fig. 7 shows a blank spot without a data point at this latitude.

With all 12 profiles lined up in Fig. 8, there is some suggestion of possible real features. The correlation method calculates the weighted average of these 12 profiles, and such averages are shown in the bottom half of Fig. 8 for the 11 rotational periods between 14.65 and 14.75 h. The averages show features of various amplitudes. For the 14.70 curve, the contrast variations are the largest, ±0.06%. Further away from 14.70, the sharpest features disappear, but the wider ones remain to some extent. At 14.65 and 14.75, average profiles are close to featureless. The remaining 789 profiles are even flatter. This is just what one expects if this zone rotates at 14.70 h and it contains a few real features.

Concerning sharpness of features or contrast rms, the 14.71 curve is next after the 14.70 curve, closely followed by the 14.69 curve. This implies that the rotational period at that latitude is between 14.70 and 14.705, and closer to 14.70 than 14.705. The correlation method takes the rms at 14.69, 14.70, and 14.71, and fits a quadratic function through these three data points, which yields a maximum rms at 14.701 h, consistent with expectations. It suggests that determining rotational periods to better than 0.01 h is easy with this method, even though the contrasts of features are 0.06% or less and no feature is clearly visible in any of the 12 profiles.

The average profiles for periods far from 14.70 h give an estimate about the noise, although the noise must be smaller than this since some contribution comes from real features. If such profiles are added to the ones near 14.70 h, it simulates how noise influences the measurement. In these simulations, the calculated maximum is typically between 14.700 and 14.702 h. Thus, the random error of the measurement is about 0.001 h.

Systematic errors can be estimated by comparing results of the correlation method with data from the feature-tracking method at the central latitudes of the 27 measured features (Table 4). The median deviation between both methods is 0.011 h. The larger deviations, however, are not due to errors, but due to the fact that the correlation method often picks up a large, strong feature that is centered on a different latitude and thus rotates with a different rate as the feature tracked.

For Fig. 8, the weighting of the Violet–Blue and Yellow spectral regions was 0.2 and 0.8 since the maximum rms signal is twice as strong in Yellow than in Violet–Blue, and the optimal weighting is proportional to the square of the signal.

Fig. 9 shows the result for all latitudes (vertical axis) and all considered rotational periods (horizontal axis). The signal strength is shown as the brightness. The color coding relates to the relative signal sizes between both spectral data. If the Violet–Blue or Yellow signal dominated, it was coded as violet or orange, respectively. If both signals were similar, it was coded as blue–green, etc. At each latitude, the location of best correlation was enhanced to guide the eye.

At latitudes near the four strongest discrete features on Uranus, the routine was not able to detect the rotational period of the second strongest feature. Thus, we ran the routine a second time after the four strongest features were hidden by interpolating pixels values between areas to the east and west of the features. Fig. 9 shows the result of both runs superposed.

The red line in Fig. 9 shows our adopted rotational profile for Uranus' southern hemisphere. It is defined in Table 5. North of −47° latitude, we adopt the profile of Sromovsky et al. (2012) since it fits our data well. Down to −59°, differences to Sromovsky's profile are minor. Between −59° and −68° latitude, the profile is almost constant, but not shown in Fig. 9 for clarity. This region is the only one coded blue. It is described in more detail in Section 6. South of −68°, the rotational period decreases steeply toward the South Polar Spot.

Fig. 9 is consistent with Fig. 7, but it provides more information. It distinguishes strong from weak features. It also shows the color and latitudinal extent of features.

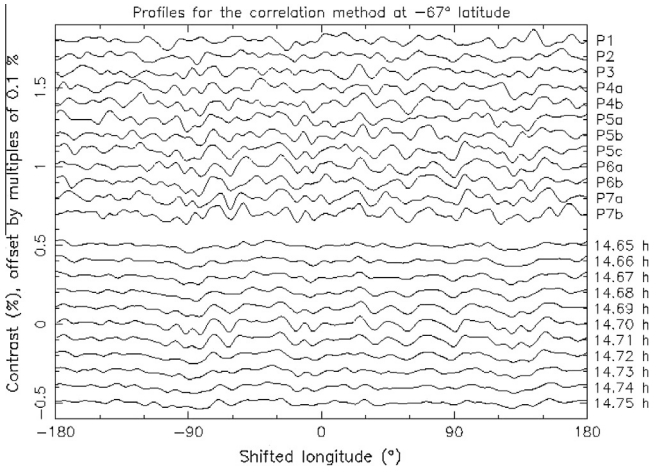

Fig. 8. Profiles of contrast versus longitude at latitude −67° for the 12 sub-periods as listed at right. Longitudes were shifted according to an assumed rotational period of 14.7 h, which means that this longitude system rotates at 14.7 h and is identical to the standard system on Jan 15.5, 1986. A weighted average of these 12 profiles is shown below in the row marked 14.70 at right. Another 10 weighted average profiles are shown for other assumed rotational periods between 14.65 and 14.75 h.

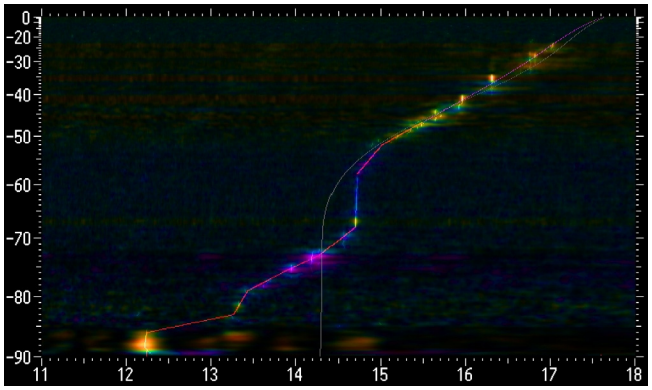

Fig. 9. Results of the correlation method. The signal is indicated by brightness for each latitude (vertical axis) and rotational period in hours (horizontal axis). The color indicates whether most of the signal comes from short or long wavelength filters. The red curve with kinks is the adopted curve, the gray, smooth curve for the mirrored northern hemisphere from Sromovsky et al. (2012). (For interpretation of the references to color in this figure legend, the reader is referred to the web version of this article.)

Table 5
Adopted rotational profile of Uranus.

Latitude (°)	Rotational period (h)
−47	15.49
−52	15.02
−58	14.72
−68	14.70
−73	14.28
−75	13.98
−79	13.44
−86	12.24
−90	12.24

Note: Linear interpolation is assumed between break points, latitudes are planetographic.

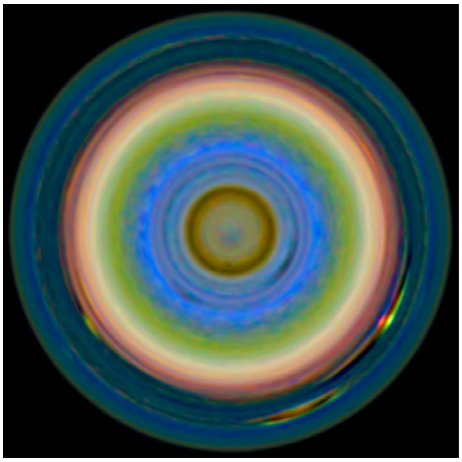

Fig. 10. Uranus as seen from above the South Pole on 1986-01-15.5 enhanced 300 times. The zero meridian is on top.

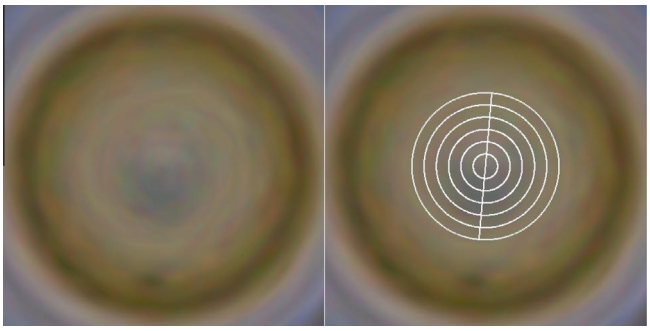

Fig. 11. The South Polar Spot (left panel, just below center) and the location of the measured profiles (right). The outer circle is at −84° latitude. The zero meridian for 1986-01-15.5 is at the top.

4.2. Spectral characteristics

The strongest features extend over several degrees of latitude, indicated in Fig. 9 by long vertical bars, often with the color of the bar varying across its extent. Thus, the assigned latitude for a feature depends on the filter. This can cause a systematic effect when trying to establish the rotational profile. Typically, the peak of the feature was further north in Yellow light than in Violet–Blue light. On the other hand, the longevity of features made uncertainties of rotational periods small and thus less important. While almost all previous rotational data came from images at red or longer wavelengths, this work provides plenty of data at shorter wavelengths.

There seem to be mainly two kinds of features. The first kind is bright spots. Their apparent contrast seems to be only dependent on the effective methane absorption coefficient (cf. Table 3). The Orange and CH4_U filters with almost identical coefficients show them similarly. These features are probably features of aerosol optical depth. They appear orange in Fig. 9.

The second kind is best visible in the Violet filter, although contrasts are similar in the noisy UV images. Toward longer wavelengths, the contrast decreases. This suggests that they are features in the aerosol scattering properties, such as aerosol absorption. At short wavelengths, aerosols on Uranus absorb more than at longer wavelengths (Karkoschka and Tomasko, 2009). Fig. 9 gives a rough idea which kind of features dominates in which latitude region.

Although the South Polar Spot appears orange in Fig. 9, its contrasts in the CH4_JS and Green filters are similar, but different in the Orange filter. This suggests it is not a feature of aerosol optical depth. Most features south of −50° latitude are of the second kind. They escaped detection for so long since observations focused on detecting the first kind of features.

Different zones display distinct spectral characteristics (Fig. 6). For the seven filters in the visible part of the spectrum, Benesh and Jepson (1978) calculated the color coordinates for the human vision. This allows creating a color image corresponding to the human vision (Fig. 10), except that the strong enhancement exaggerates color contrasts as well as intensity contrasts. Without enhancement, Uranus is a blue–green disk with barely one visible feature.

5. South Polar Spot

5.1. Longitude measurements

The South Polar Spot is a dark spot containing Uranus' South Pole (Fig. 11). It rotates 2 h faster than expected from the rotational profile of Sromovsky et al. (2012), the only feature off by more than 1 h from Sromovsky's.

At latitudes close to the South Pole, the intensity varied with longitude roughly as a sine curve. A routine measured the phase and amplitude of the sine curve by a least square fit. The minimum of the fitted sine curve was taken as the longitude of the spot. Best suited were the 12 subdivided periods with all filters averaged using latitudes −89° to −86°.

The 12 measured longitudes are shown in Fig. 12 (top panel). The short-term motion is best visible during periods P4–P7. Between period P1 and P7, the interior of Uranus rotated 50 times, while the South Polar Spot added 20 rotations for a total of 70 rotations. The least-square fit has a rotational period of 12.24 h with a precision of 0.012 h. Considering systematic errors of similar magnitude, a total uncertainty of 0.02 h is adopted here.

Residuals of the measurements with respect to the best fit are shown in the bottom panel of Fig. 12 as solid dots. Open circles show measurements with the same routine and similar accuracy, except that the latitude range was changed to −87° to −85°. Most open and solid circles are consistent. However, the first and last data points in period P5, are off by 4 sigma. At those times, the northern part of the South Polar Spot was irregular near −86° latitude. Some temporal disturbance must have happened. The South Polar Spot may have also had a variation during period P6, but the deviations are only 2–3 sigma and thus less significant.

Note that the open circle for period P1 is not visible in Fig. 12 since the data point is only 1° off from the solid dot. This must be a coincidence since such a difference corresponds to an offset of only 0.03 pixels in original images.

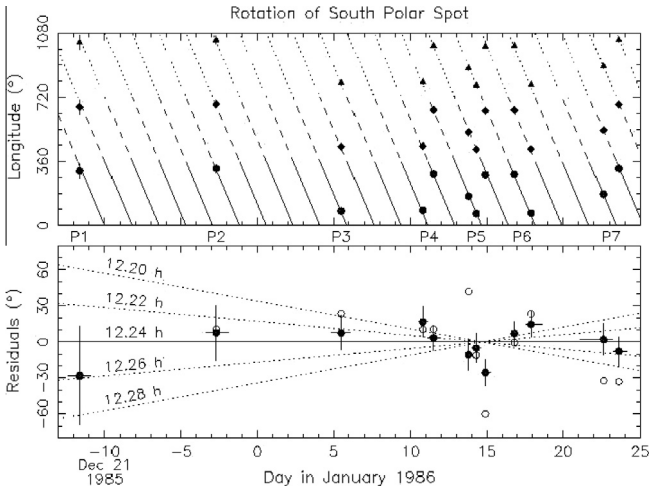

Fig. 12. Longitude measurements of the South Polar Spot. The top panel has the full range of longitudes (0–360°) wrapped around three times so that the spot can be followed over intervals of several days. The bottom panel displays longitudes relative to the best fitting constant motion, the solid line. Dotted lines indicate motions corresponding to slightly different rotational periods with the same longitude on January 14, 1986. Solid and open circles indicate measurements −89° to −86° and −87° to −85°, respectively. Vertical bars are error bars for the solid dots. Horizontal bars show the extent of each observing period. Main periods are listed between both panels.

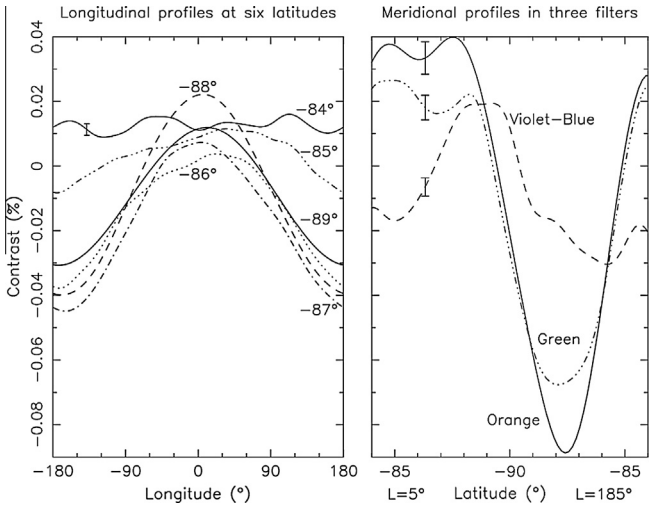

Fig. 13. Longitudinal contrast profiles of the South Polar Spot at six latitudes (left panel) and meridional profiles in three spectral bands (right panel). The selected meridian is the spot's longitude of 185° on the standard date 1986-01-15.5, switching to the 5° meridian on the other side (left) of the South Pole. Sample error bars are indicated.

Near the South Pole, the correlation method (Fig. 9) shows secondary signal maxima for rotational periods near 13.3 and 14.8 h. These periods correspond to one rotation less every 6 days and 3 days, respectively. These periods fit some of the data since the spacing between several pairs of observations is close to multiples of 6 days. However, in the top panel of Fig. 12, lines with a very different slope than shown clearly do not fit the data of periods P4–P6. At least one data point would be off by more than 90° in longitude. Thus, the weak secondary maxima from the correlation method can be eliminated with very high confidence level.

5.2. Shape and contrast

We averaged all 1600 images according to a 12.24 h rotational period. Zonal contrast profiles are shown in Fig. 13 (left panel). For this plot, 1°-wide ranges of latitude and 50°-long ranges of longitudes were averaged. The latitude bin of the South Pole would plot close to the zero-percent level. The locations of the six profiles are indicated by the six circles in Fig. 11. The four profiles closest to the South Pole are similar to sine curves with peak-to-peak amplitudes of 0.05–0.06%. At −85°, the amplitude is three times smaller.

At −84°, no signal of the Solar Polar Spot is visible, and the data look like noise. For this curve the rms deviation from its mean is 0.0018%, or 18 ppm (ppm), or 1 part in 55,000. Each data point on this curve is an average over 80,000 original data points, 1600 images and about 50 pixels per image on average. Thus, the signal-to-noise ratio of this curve should be square-root of 80,000 = 280 times higher than the signal-to-noise ratio of each original data point, which is about 200. So a noise level of 1 part in 56,000 or 18 ppm is expected. The fact that measured variations are very similar suggests that systematic variations and real features on Uranus are most likely well below that level, on the order of 10 ppm or less. Mixing within this latitude must be very effective compared to processes that create features. Few reflectivities in nature have been measured to this level of precision.

A couple of other latitudes in the Voyager data set come close to the blandness of the −84° region, but most latitudes show significant features that can be tracked. Northward of −20°, images also appear featureless, but these latitudes remained close to the limb where strong intensity gradients decrease the achievable precision.

By comparison, detecting small extrasolar planets with the transit method requires similar precision as detecting features at some latitudes on Uranus. For example, the Kepler spacecraft has provided transit depth data with a median precision of 29 ppm (Gilliland et al., 2011). Transit depth as function of wavelength has been measured to a similar precision, for example obtaining a featureless spectrum to the 30 ppm level (Kreidberg et al., 2014).

Meridional profiles of the South Polar Spot are shown in the right panel of Fig. 13. The location of the cut across the South Pole is shown by the almost vertical line in Fig. 11. The Violet, Clear, and Blue filters show similar profiles, so just their average is displayed. The Green and Orange filters display profiles of similar shape, but different amplitude, 0.09% (Green) and 0.12% (Orange). The steep sections in both filters are aligned to 0.1° in latitude, the minima occur between −88° and −87.5° latitude. The spot's FWHM was 4° and the total width was 6–7°. A spot containing the pole near its edge is unique among jovian planets.

At shorter wavelengths, the dark spot is almost gone, except perhaps a little 0.01% dip near −86° latitude, but a bright spot appears on the other side of the South Pole.

In summary, the South Polar Spot rotated at 12.24 ± 0.02 h. It showed a variety of temporal, spatial, and spectral characteristics with contrasts on the order of 0.01–0.1% that provide many constraints for future, physical interpretations.

The regions around the South Poles of Saturn and Neptune have also revealed surprising features. At Saturn, a dark area is centered on the South Pole, unlike the off-center South Polar Spot, but it also rotates much faster than the interior (Dyudina et al., 2009), similar to the case at Uranus. At Neptune, small, bright spots were detected near −88° and −89° latitude (Luszsz-Cook et al., 2010). The rotation near the South Pole is also peculiar. While Uranus and Neptune have long rotational periods at the equator gradually decreasing to short rotational periods at high latitudes, this trend reverses at −80° latitude at Neptune with the South Pole rotating almost as slowly as the equator (Karkoschka, 2011). Thus, Uranus and Neptune both have steep rotational profiles near each South Pole, but the slopes are of opposite sign.

Considering these anomalies near the poles, the rotational profile of Sromovsky et al. (2012) is uncertain near the North Pole

since none of their data extend beyond 78° latitude. Thus, the asymmetry beyond 78° is also uncertain (Fig. 2). For example, if Uranus' rotation near the North Pole would follow Neptune's near its South Pole, the asymmetry would go up to about 40%, more than twice as much as displayed in Fig. 2. Perhaps, Jupiter's decrease of wind speeds toward the poles is unique among jovian planets, and significant wind speeds measured near the poles at other jovian planets are typical, leading to large deviations in rotational periods.

6. Low-Shear Region

The region between −68° and −59° latitude rotates almost like a solid body and is thus called the Low-Shear Region. Inside this region, the slope of the rotational profile is about 30 times lower than outside (Fig. 14). Both transition regions seem to be quite small, causing two kinks in the profile that was considered smooth previously. A smooth profile suggested a simple dynamical system with perhaps one Hadley cell at each hemisphere, transferring angular momentum from the slowly rotating equator to the faster rotating high latitudes with almost perfect north–south symmetry. The two kinks suggest a more complicated system.

The Low-Shear Region has no strong features (Fig. 15). Any feature with ±0.1% contrast would saturate white or black due to 1000-fold contrast enhancement, but none comes close to it. If Uranus would rotate perfectly as a solid body, the three images for periods P4, P5, and P6 could be averaged without smearing features, which is almost the case. A comparison of the average image (bottom of Fig. 15) with the other three shows good correlations for the stronger features, but the details do not match due to the 1000-fold enhanced noise.

The black lines in Fig. 15 show the shear due to our adopted rotational profile for a meridian in period P5. The strong shear outside the Low-Shear Region moves the dark spot near the bottom left further left. Thus, it is smeared in the average (bottom of Fig. 15).

Even with the lack of strong features, the correlation method gives accurate results. Within the region, the rotational period is 14.709 h with an rms of 0.0065 h. With a linear fit, the rms goes down to 0.0010 h (Fig. 14), indicating that the slope is highly significant. The linear fit has rotational periods of 14.698 h and 14.720 h at −68° and −59° latitude, respectively. Linear fits to 9°-wide, adjacent regions north and south have 38 and 25 times

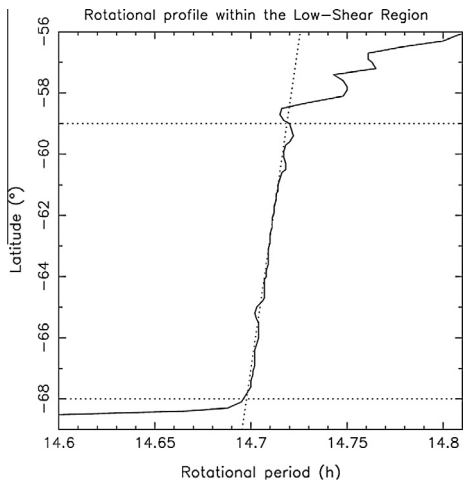

Fig. 14. Rotational profile within the Low-Shear Region (solid curve) based on the best fit from the correlation method. Horizontal lines indicate the approximate vertical extent of the region. The slanted dotted line is a linear fit within the region.

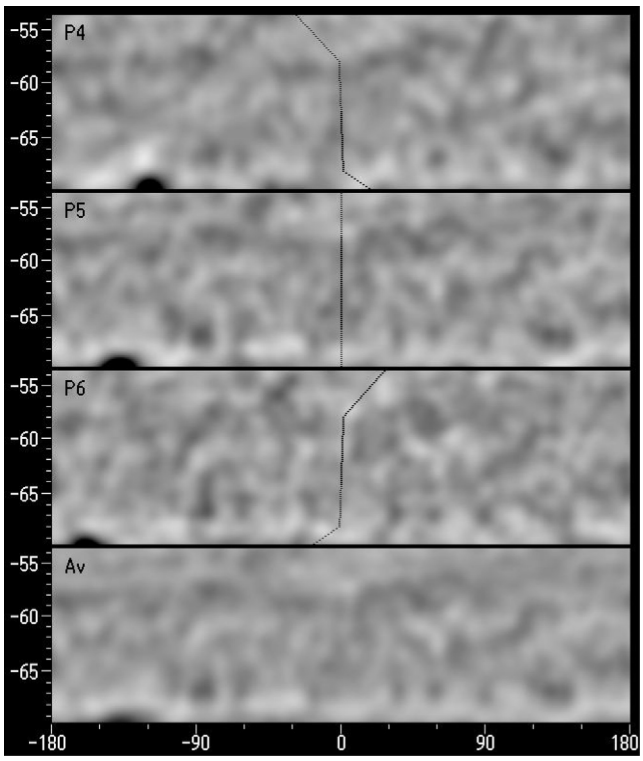

Fig. 15. The Low-Shear Region in three periods (P4–P6) and the average. Longitudes are aligned using a rotational period of 14.71 h. Contrasts are enhanced 1000 times.

larger slopes, respectively. The rms of 0.0010 h is consistent with noise as estimated in Section 4 for the profiles shown in Fig. 8.

This small rms of 0.0010 h from a linear fit over 9° of latitude is remarkable. It corresponds to a wind speed of about 0.1 m/s in a region with wind speeds above 200 m/s with respect to the interior rotation. Even regions of jovian planets with much lower wind speeds do not display such regular behavior.

It is interesting to note that Sromovsky et al. (2012) found a region between 62° and 78° latitude that may be similar to the Low-Shear Region, Based on tracking 12 features, its rotational period is 14.3 h with individual measurements scattering about 0.3 h around this value. The scatter is consistent with random errors that are much larger than for the Low-Shear Region since the observation period was only 53 h long. A small slope in the rotational profile like that of the Low-Shear Region cannot be excluded by the data. There are no data to distinguish between a rotational profile with a kink or a smooth transition. More accurate data are needed to check whether this region is similar to the Low-Shear Region.

7. Spirals

Zonal features are common on the jovian planets, and Uranus has plenty. Some features may look like zonal features, but closer investigation of Fig. 6 reveals that they are not zonal but slightly inclined with respect to latitude circles. They run from bottom left to top right. Examples are the dark, long feature near −30° latitude and the shorter, brighter, parallel streaks near −45°. They are best visible in the Green and Orange filters, but can be traced in most other filters (Fig. 6). The dark feature can be traced over more than 360° in longitude. The "head" runs parallel to the "tail" with a separation of 3–4° during early periods, decreasing to 2–3° later. In unprojected images, these features are tightly wound spirals.

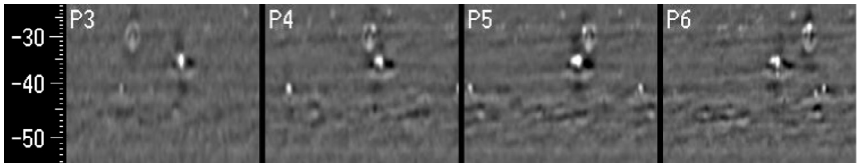

Fig. 16. The mid-southern latitudes during periods P3–P6. Long features that are tilted with respect to horizontal latitude circles are called spirals. As time progresses, they wind up and align closer to the zonal direction. Longitudes between the four panels are aligned according to a rotational period of 16.31 h, corresponding to the actual rotational period at −37° latitude. Features further north and south move to the right and left, respectively.

These spirals are located in regions with major rotational shear. Fig. 16 shows their temporal evolution in Yellow images of periods P3–P6 with a projection identical to that of Fig. 6. For all spirals, the angle gets shallower with time due to differential rotation. The dark spiral in the north was already tightly wound up in period P3. Based on measured angles and the known rotational shear, this spiral might have been aligned with meridians around the beginning of December, 1985, invisible to Voyager. The lack of irregularities after 50 days sets an upper limit on turbulence or differences in meridional motions. North–south irregularities larger than 100 km would be noticeable, and 100 km in 50 days is an average speed of 2 cm/s. The spiral was perfectly aligned with the spot at −29° latitude, suggesting that it is connected with that spot. Although the spiral was dark, its northern edge was bright compared to surroundings.

The spirals further south were not wound up as much, suggesting they were younger. Perhaps, they formed during the early periods such as P1 or P2, when Voyager's resolution was limited. Note that our processing creates dark halos around bright features that are compressed into dark vertical streaks in projections such as Fig. 16, not to be confused with real features.

8. Animations

Time-lapse animations of the rotation of planets are a different way to comprehend rotational shear. We created three animations that are available in the on-line Supplemental material. All three required the results of this work for Uranus' rotation.

The first animation displays 30 h of rotation in 30 s. The surroundings of Uranus are a mosaic from six WAC images on 1986-01-23. The inner satellites are shifted according to known rotation periods. The beginning of the animation shows a true-color disk of Uranus that outshines the ring, satellites, and stars of Sagittarius.

The second animation shows Uranus from a view above the South Pole. The viewer co-rotates with Uranus, first at a 18 h rotational period, which is slower than Uranus, then accelerating to a rotational period of 12 h, which is even faster than the South Polar Spot.

The third animation shows a 2-day rotation for all planets with a viewing angle at winter solstice. A coordinate grid represents the interior while an initial color coding with longitude represents the atmosphere. The data come from Hueso et al. (2007) for Venus, Marshall and Plumb (2007) for the Earth, Sonnabend et al. (2006) for Mars, and otherwise as for Fig. 1.

9. Summary

We analyzed the calibration procedures for Voyager images of Uranus and improved several systematic and random errors that were on the order of 1–10%, which may be negligible for most Solar System objects, but not for Uranus. We averaged 1600 images of Uranus in various ways to detect new features. Our results are:

1. North of −45° latitude, the rotational profile of Uranus was well constrained by observations taken between 1997 and 2011 (Sromovsky et al., 2012). Our data of 1985/1986 extending up to −20° indicate no significant temporal change over 25 years of observations.
2. South of −45° latitude, only one feature was known so far (Smith et al., 1986). We found dozens of features covering this whole region with no gap larger than 3°. Down to −57°, our profile is close to Sromovsky's, but not further south.
3. South of −57° latitude, Uranus' rotational profile is highly asymmetric with respect to the northern hemisphere's profile, more asymmetric than for all previous data of jovian planets. This result supports the notion that winds on both hemispheres are not connected through the interior and have limited depth (Kaspi et al., 2013).
4. North of −73° latitude, the southern hemisphere rotated slower than the northern one, but faster further south. The strong asymmetry was hidden since the only feature known before was right at −73°.
5. Between −59° and −68° latitude, Uranus' atmosphere rotated almost like a solid body with rotational shear about 30 times less than further north and south. Such a variation with sharp kinks is unique. The regular rotation within this region to 0.1 m/s is far below wind speeds of 200 m/s and defies current ideas of Uranus' circulation.
6. A dark spot contained the South Pole off center. It rotated with a 12.24 h rotational period, which is 2 h faster than the fastest uranian feature known before and 5 h faster than the interior rotation, the largest such difference known among jovian planets, although the regions around the South Poles of Saturn and Neptune also have unusual rotational profiles.
7. We detected tightly wound spirals, some encircling the planet more than once. Voyager watched their evolution due to rotational shear. Their regular shape suggests meridional wind speed variations of no more than 2 cm/s.
8. Uranus displayed zonal structure with a rich spectral variety. Discrete features were roughly categorized into two spectral groups, one likely due to variations in aerosol optical depth, and one due to variations in aerosol absorption. Almost all features known before belong to the first group since observations focused on longer wavelengths. The region south of −45° latitude had no features of the first group and thus had no reliable rotational profile before this work.
9. The zone at −84° latitude displayed reflectivity variations of only 18 ppm that are due to noise since the signal-to-noise ratio was estimated at 55,000. This zone is one of the blandest areas in nature ever measured.

This first work with a recalibrated data set focused on feature detection. Physical interpretation of features is a future goal that is well constrained by spectral characteristics revealed here. We plan to make the processed images of Uranus available at NASA's Ring-PDS.

Some of our calibration improvements may also be suitable for other Voyager images, such as the 5–10% adjustment in the nonlin-

ear detector response. Perhaps, this may improve absolute response calibration from roughly the 10% level (Danielson et al., 1981) closer to the ~1% stability of the detectors. Voyager images of the Uranus and Neptune systems are unlikely to get surpassed with respect to spatial resolution during the next 20 or 30 years.

Acknowledgments

This work was supported by NASA grant NNX12AI68G. Mark Showalter provided help and valuable information about the Voyager images on the PDS.

Appendix A. Supplementary material

Supplementary data associated with this article can be found, in the online version, at http://dx.doi.org/10.1016/j.icarus.2014.12.003.

References

Barnet, C.D., Westphal, J.A., Beebe, R.F., Huber, L.F., 1992. Hubble Space Telescope observations of the 1990 equatorial disturbance on Saturn: Zonal winds and central meridian albedos. Icarus 100, 499–511.
Barrado-Izagirre, N., Sánchez-Lavega, A., Pérez-Hoyos, S., Hueso, R., 2008. Jupiter's polar clouds and waves from Cassini and HST images: 1993–2006. Icarus 194, 173–185.
Benesh, M., Jepson, P., 1978. Voyager Imaging Science Subsystem Calibration Report. Jet Propulsion Laboratory, Pasadena.
Danielson, G.E., Kupferman, P.N., Johnson, T.V., Soderblom, L.A., 1981. Radiometric performance of the Voyager cameras. J. Geophys. Res. 86, 8683–8689.
Dyudina, U.A. et al., 2009. Saturn's south polar vortex compared to other large vortices in the Solar System. Icarus 202, 240–248.
García-Melendo, E., Pérez-Hoyos, S., Sánchez-Lavega, A., Hueso, R., 2011. Saturn's zonal wind profile in 2004–2009 from Cassini ISS images and its long-term variability. Icarus 215, 62–74.
Gilliland, R.L. et al., 2011. Kepler mission stellar and instrument noise properties. Astrophys. J. Suppl. 197 (1), id. 6.
Hammel, H.B., 1997. Winds of change on Uranus? Bull. Am. Astron. Soc. 29, 994.
Hueso, R., Pérez-Hoyos, S., Sánchez-Lavega, A., Peralta, J., 2007. The atmosphere of Venus: Winds and clouds observed by VIRTIS/Venus Express. In: Ulla, A., Mantaiga, M. (Eds.), Lecture Notes and Essays in Astrophysics, vol. 3. Turculo Press, Spain.
Karkoschka, E., 1997. Rings and satellites of Uranus: Colorful and not so dark. Icarus 125, 348–363.
Karkoschka, E., 1998. Clouds of high contrast on Uranus. Science 280, 570–572.
Karkoschka, E., 2001. Uranus' apparent seasonal variability in 25 HST filters. Icarus 151, 84–92.
Karkoschka, E., 2011. Neptune's rotational period suggested by the extraordinary stability of two features. Icarus 215, 439–448.
Karkoschka, E., Tomasko, M., 2009. The haze and methane distribution on Uranus from HST-STIS spectroscopy. Icarus 202, 287–309.
Kaspi, Y., Showman, A.P., Hubbard, W.B., Aharonson, O., Helled, R., 2013. Atmospheric confinement of jet streams on Uranus and Neptune. Nature 497, 344–347.
Kreidberg, L. et al., 2014. Clouds in the atmosphere of the super-Earth exoplanet GJ1214b. Nature 505, 69–72.
Limaye, S.S., 1986. Jupiter: New estimates of the mean zonal flow at cloud level. Icarus 65, 335–352.
Limaye, S.S., Sromovsky, L.A., 1991. Winds of Neptune: Voyager's observations of cloud motions. J. Geophys. Res. 96, 18941–18960.
Luszsz-Cook, S.H., de Pater, I., Ádámkovics, M., Hammel, H.B., 2010. Seeing double at Neptune's South Pole. Icarus 208, 938–944.
Marshall, J., Plumb, R.A., 2007. Atmosphere, Ocean, and Climate Dynamics. Elsevier Academic Press, Burlington, Texas.
Showalter, M.R., Gordon, M.K., Olson, D., 2013. VG2 Uranus ISS processed images V1.0, VGISS_7201-7207. NASA Planetary Data System.
Simon-Miller, A.A., Gierasch, P.J., 2010. On the long-term variability of Jupiter's winds and brightness as observed from Hubble. Icarus 210, 258–269.
Smith, B.A. et al., 1986. Voyager 2 in the uranian system: Imaging science results. Science 233, 43–64.
Sonnabend, G., Sornig, M., Krötz, P.J., Schieder, R.T., Fast, K.E., 2006. High spatial resolution mapping of Mars mesospheric zonal winds by infrared heterodyne spectroscopy of CO_2. Geophys. Res. Lett. 33, L18201.
Sromovsky, L.A., Fry, P.M., 2005. Dynamics of cloud features on Uranus. Icarus 179, 459–484.
Sromovsky, L.A., Limaye, S.S., Fry, P.M., 1995. Clouds and circulation on Neptune: Implications of 1991 HST observations. Icarus 118, 25–38.
Sromovsky, L.A., Spencer, J.R., Baines, K.H., Fry, P.M., 2000. Note: Ground-based observations of cloud features on Uranus. Icarus 146, 307–311.
Sromovsky, L.A., Fry, P.M., Hammel, H.B., Ahue, W.M., de Pater, I., Rages, K.A., Showalter, M.R., van Dam, M.A., 2009. Uranus at equinox: Cloud morphology and dynamics. Icarus 203, 265–286.
Sromovsky, L.A., Fry, P.M., Hammel, H.B., de Pater, I., Rages, K.A., 2012. Post-equinox dynamics and polar cloud structure on Uranus. Icarus 220, 694–712.
Warwick, J.W. et al., 1986. Voyager 2 radio observations of Uranus. Science 233, 102–106.